Effects of MJO Vertically Tilted Structure on Its Phase Speed from the Moisture Mode Theory Perspective

FENG HU[a] AND TIM LI[b,a]

[a] *Key Laboratory of Meteorological Disaster, Ministry of Education/Joint International Research Laboratory of Climate and Environmental Change/Collaborative Innovation Center on Forecast and Evaluation of Meteorological Disasters, Nanjing University of Information Science and Technology, Nanjing, China*
[b] *Department of Atmospheric Sciences, School of Ocean and Earth Science and Technology, University of Hawai'i at Mānoa, Honolulu, Hawaii*

(Manuscript received 16 September 2020, in final form 25 February 2021)

ABSTRACT: The effect of vertically tilted structure (VTS) of the MJO on its phase propagation speed was investigated through the diagnosis of ERA-Interim reanalysis data during 1979–2012. A total of 84 eastward propagating MJO events were selected. It was found that all MJO events averaged throughout their life cycles exhibited a clear VTS, and the tilting strength was significantly positively correlated to the phase speed. The physical mechanism through which the VTS influenced the phase speed was investigated. On the one hand, a stronger VTS led to a stronger vertical overturning circulation and a stronger descent in the front, which caused a greater positive moist static energy (MSE) tendency in situ through enhanced vertical MSE advection. The stronger MSE tendency gradient led to a faster eastward phase speed. On the other hand, the enhanced overturning circulation in front of MJO convection led to a stronger easterly/low pressure anomaly at the top of the boundary layer, which induced a stronger boundary layer convergence and stronger ascent in the lower troposphere. This strengthened the boundary layer moisture asymmetry and favored a faster eastward propagation speed.

KEYWORDS: Madden-Julian oscillation; Moisture/moisture budget

1. Introduction

The Madden–Julian oscillation (MJO; Madden and Julian 1971, 1972) is a dominant mode on the intraseasonal time scale in the tropics. Although the MJO main convection is confined in the tropics, it may exert a remote impact in the high latitudes (e.g., Zhang 2005; Li and Hsu 2017; Zhu and Li 2017; Ren et al. 2018; Li et al. 2020). The most fundamental characteristic of the MJO is its slow eastward propagation at approximately $5\,m\,s^{-1}$ along the equator with a planetary zonal scale (e.g., Knutson et al. 1986; Lau and Chan 1986; Hendon and Salby 1994; Wheeler and Kiladis 1999; Kiladis et al. 2009; Li and Zhou 2009; Lau and Lau 2010; Li 2014).

Various theories (e.g., Emanuel 1987; Wang and Rui 1990) have been developed to understand the MJO eastward propagation. The most recent widely accepted one is the moisture mode theory, which emphasizes the important role of MJO-scale moisture perturbation in the propagation dynamics (e.g., Maloney 2009; Hsu and Li 2012; Sobel and Maloney 2012, 2013; Adames and Kim 2016; Kim and Maloney 2017; Maloney et al. 2019). The moisture mode theory may be further separated into two types, based on their physical origins (Hu et al. 2020; Li et al. 2020; Wang and Li 2020b). The first type emphasizes the zonal asymmetry of the perturbation moisture itself (Hsu and Li 2012). The perturbation moisture in the planetary boundary layer (PBL) leads the MJO convection. Such a phase leading was caused by the advection of the mean moisture by anomalous ascent associated with the PBL convergence according to a moisture budget analysis. The PBL convergence in front of MJO convection, on the other hand, was a result of an MJO heating-induced Kelvin wave response and a warm SST anomaly in front of the convection (Hsu and Li 2012). The PBL moistening gradually set up local convective instability and triggered shallow and congestus convection (Benedict and Randall 2007; Johnson and Ciesielski 2013), promoting the eastward propagation of the MJO. The PBL moistening and congestus clouds developing processes were well documented by various observational studies (e.g., Johnson et al. 1999; Kikuchi and Takayabu 2004; Del Genio et al. 2012), including those during the DYNAMO observational campaign (Johnson and Ciesielski 2013). There was clearly stepwise progression from shallow cumulus to congestus and to deep convection. This PBL moisture asymmetry mechanism was well incorporated into a simple theoretical model (Liu and Wang 2017; Wang and Chen 2017) with a simplified Betts–Miller cumulus scheme in which diabatic heating was proportional to lower-tropospheric and PBL moisture anomalies, and the model was able to simulate a slowly eastward propagating MJO-like perturbation.

The second type of the moisture mode theory emphasizes the zonal asymmetry of the column-integrated moisture or moist static energy (MSE) tendency, regardless of whether or not the PBL perturbation moisture itself is asymmetric. Sobel and Maloney (2012, 2013) established a simple theoretical model using a column-integrated specific humidity tendency equation. The phase speed of the most unstable mode derived from this model, however, was too slow compared to the observed. A MSE budget analysis by Andersen and Kuang (2012) suggested that vertical and horizontal advection is critical for promoting a zonally asymmetric MSE tendency. Adames and Kim (2016) improved the model of Sobel and Maloney (2013) by including a meridional advection mechanism proposed by Kim et al. (2014).

Corresponding author: Tim Li, timli@hawaii.edu

DOI: 10.1175/JCLI-D-20-0732.1

Recently, Li and Hu (2019) further extended this theoretical framework by including an additional mechanism, anomalous vertical MSE advection by second-baroclinic-mode vertical motion proposed by Wang et al. (2017).

The moisture mode theoretical framework has been applied to observational and model diagnosis. It is worth mentioning that current state-of-art general circulation models (GCMs) have difficulty in capturing the eastward propagation of the MJO. For example, by analyzing 27 global GCMs that participated in the Working Group on Numerical Experimentation (WGNE) MJO Task Force–GEWEX Atmospheric System Studies (MJOTF/GASS) model intercomparison project, Jiang et al. (2015) proposed that only about a quarter of the models were able to simulate the realistic eastward propagation. Based on the profile of vertical velocity and diabatic heating, they found the existence of vertically tilted structure (VTS). Through deeper diagnosis of the MSE budget within the moisture mode framework, Wang et al. (2017) further found that the fundamental difference between the good model group and the poor model group lay in the presence of the VTS. While a low-level ascent appeared in front of MJO convection, an upper-level ascent appeared to the rear of the MJO convection. Such a tilting structure was found in both the observation and the good model group, but not in the poor model group. The upper-level ascent in the rear was closely associated with a positive diabatic heating in situ, implying the occurrence of upper-tropospheric stratiform clouds in the rear. The importance of the VTS and/or upper-tropospheric stratiform clouds was stressed in various previous observational and modeling studies (e.g., Mapes 2000; Khouider and Majda 2008; Fu and Wang 2009; Zhang and Song 2009).

Wang et al. (2019) classified MJO events into four groups (standing, jumping, slow propagation, and fast propagation) by cluster analysis. They found that each type of MJO exhibited distinctively vertical structure. The faster propagation MJO group was occupied by stronger and longer low-level Kelvin wave response. Chen and Wang (2020) then analyzed the mechanism deeply. By amplifying low-level premoistening, a stronger Kelvin wave response enhanced the zonal asymmetry in vertical thermal structures, as manifested by the enhanced leading shallow and congestus convection. This view is consistent with the first moisture mode theory, but without the direct description and consideration of the second moisture mode theory. Also, their emphasis was the vertical structure to the east of MJO, while the vertical tilted structure in the rear was not considered.

Motivated by the aforementioned studies, we would like to examine to what extent the VTS in the rear happens in the observed eastward propagating MJO events and what is the statistical relationship between the VTS and phase speed for a large number of MJO events. If a statistically significant relationship is found, what is the physical mechanism behind the observed relationship? The remaining part of this paper is organized as follows. In section 2, data and methods are introduced. In section 3, the observational features of the VTS for individual MJO events are presented and their statistically significant relationship with the phase speed is revealed. The physical mechanism behind the observed relationship is further investigated under the moisture mode theoretical framework in section 4. Finally, conclusions and discussion are given in the last section.

2. Data and method

a. Data

The primary datasets used in this study are daily observed outgoing longwave radiation (OLR) from the National Oceanic and Atmospheric Administration (NOAA) polar-orbiting satellites (Liebmann and Smith 1996) with a horizontal resolution of 2.5° × 2.5°, and daily reanalysis data from ECMWF interim reanalysis (ERA-Interim, herein ERA-I; Dee et al. 2011) including air temperature, specific humidity, geopotential height, horizontal wind, vertical pressure velocity, and surface heat fluxes with a horizontal resolution of 1.5° × 1.5°. The analysis period covers the boreal winter season from 1 November to 30 April for a 33-yr period (1979–2012).

b. Selection of MJO events

A multivariate empirical orthogonal function (MV-EOF) is used for eastward propagating MJO events selection, similar to Wheeler and Hendon (2004). Before calculating the leading MV-EOF patterns, a 20–100-day Lanczos bandpass filtering is applied to the OLR and upper and lower tropospheric zonal wind fields. The leading two MV-EOF modes show strong convective centers over the tropical eastern Indian Ocean and the western Pacific respectively, and the combination of the two modes represent the eastward propagation of the MJO convection. Reconstructing the OLR anomaly field by regressing original OLR field onto the normalized aforementioned first and second MV-EOF time series, one may obtain the eastward propagating OLR signal.

Followed Zhang and Ling (2017), criteria are defined for the selection of the MJO events to remove weak events with short duration: 1) the reconstructed OLR anomaly is less than or equal to $-15\,\mathrm{W\,m^{-2}}$, 2) the OLR contour with the aforementioned strength must move continually across 50° in longitude and over the Indian Ocean and the Maritime Continent (MC), and 3) all MJO daily samples are confined between 60°E and 180°. The reasons why we have not considered short-duration MJO events here is that Feng et al. (2015) proposed different propagating mechanisms for propagating and nonpropagating MJO events over the MC. Besides, MJO events are usually slowed down by MC and the phase speed is different between the Indian Ocean and Pacific Ocean, which would make the result complicated when we compare faster and slower propagating MJO events.

With the criteria above, a total of 84 MJO events are selected during the 33-yr period. On average, about 2.5 MJO events happen within a year. Figure 1a shows the time–longitude section of the OLR anomaly during the 2003/04 winter as an example. As one can see, the selected MJO events are strong and move steadily eastward. To describe associated MJO-scale circulation patterns, all reanalysis fields are reconstructed based on the two leading MV-EOF time series. Note that all fields are normalized, which represents that the comparison is done based on the same MJO strength. Taking the moisture field as an example, the specific method of normalization is dividing the moisture by MJO intensity for every

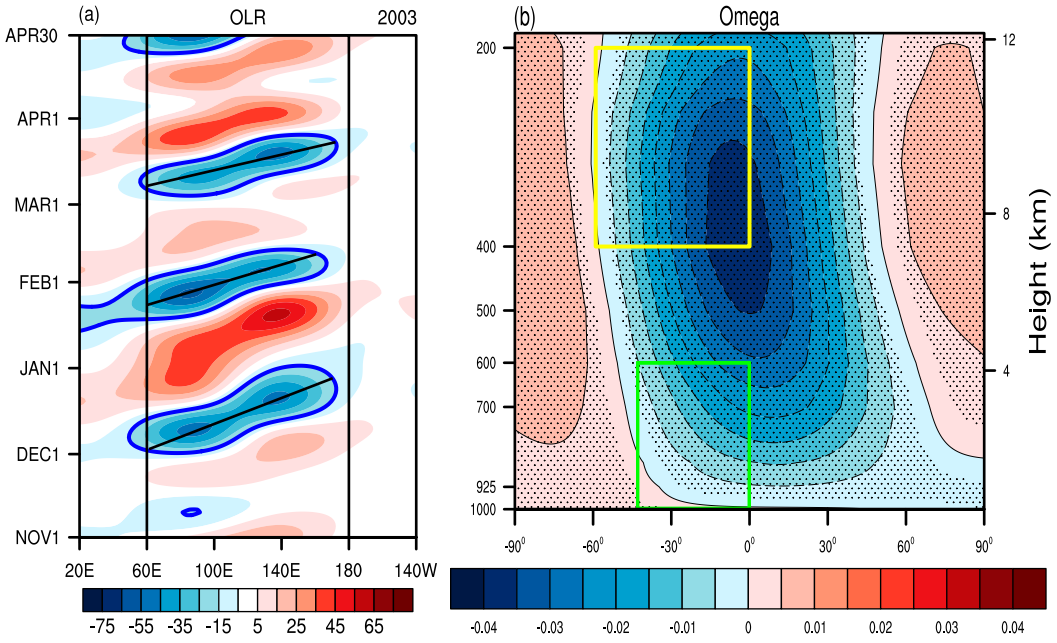

FIG. 1. (a) Hovmöller diagram of reconstructed OLR anomalies (W m^{-2}) averaged between 15°S and 15°N during the 2003/04 winter. The blue contour denotes the -15 W m^{-2} contour. The black line is based on a least squares fit, which is used to estimate the average phase speed. The longitudinal range under consideration is outlined in black lines. (b) Vertical–zonal cross section of anomalous vertical velocity field (Pa s^{-1}), averaged between 15° south and north to the MJO convective center, composed based on the total 84 MJO cases. The x axis represents the relative longitude to the MJO convective center. Yellow and green boxes represent the zonal extent of anomalous ascent in the upper and lower troposphere, respectively. Dotted areas exceed a 95% confidence level with the Student's t test.

MJO events. The average phase speed of each MJO event is calculated based on the slope of a least squares fit line of the MJO convective centers.

c. *Definition of a VTS index*

The intensity of the VTS is defined as the difference of longitudinal extent of box-averaged ascent anomaly between the upper troposphere and the lower troposphere in the rear of the MJO convection, as illustrated in the composite pattern of vertical p-velocity anomaly field (Fig. 1b). There is a clear westward vertical tilting with height in the vertical velocity field. Upward motion anomalies appear in the upper troposphere in the rear, whereas they appear in the lower troposphere in the front. The diabatic heating anomaly exhibits a similar pattern (figure not shown; see Wang et al. 2017).

The yellow box in Fig. 1b denotes the longitudinal extent of the ascent anomaly in the upper troposphere (400–200 hPa), measuring how far it is from the MJO convective center. The green box denotes the longitudinal extent of the ascent anomaly in the lower troposphere (1000–600 hPa). Here the MJO convective center is the longitude where the strongest negative OLR anomaly (averaged over 15°S–15°N) is located. The tilting intensity index is defined as the difference of longitudinal extent of ascent anomaly between the lower (green box in Fig. 1b) and upper troposphere (yellow box in Fig. 1b). For an MJO event it is calculated as the VTS intensity averaged during the entire MJO life cycle. A positive value of the index represents that the MJO-scale ascending motion is tilted westward with height. A larger tilting intensity index indicates a stronger tilted vertical structure. A similar definition of the diabatic heating anomaly is applied to verify the robustness of the index based on vertical velocity. The correlation coefficient between the tilting intensity index based on vertical velocity and diabatic heating is 0.72, exceeding the 99% confidence level with the Student's t test. Therefore, in the following analysis, the VTS index based on vertical velocity is used.

d. *Moisture budget diagnosis*

To understand the effect of the VTS on MJO phase speed from the perspective of the first type of moisture mode theory, a moisture budget diagnosis is applied. Following Yanai et al. (1973), the moisture tendency equation on the intraseasonal time scale can be written as

$$\partial_t q' = -(u\partial_x q)' - (v\partial_y q)' - (\omega\partial_p q)' - Q_2'/L, \qquad (1)$$

where a prime denotes reconstructed variables, q represents the specific humidity, and u, v, and ω are zonal, meridional, and vertical velocity, respectively. The term Q_2 is the apparent moisture sink, and L (2.5×10^6 J kg^{-1}) is the latent heat of condensation. The first, second, and third terms on the right-hand side (rhs) of Eq. (1) are zonal, meridional, and vertical moisture advection, respectively. The fourth term denotes the moisture changing rate due to condensational heating.

The average PBL operator from 1000 to 700 hPa is applied to the budget equation to diagnose the relative contribution of

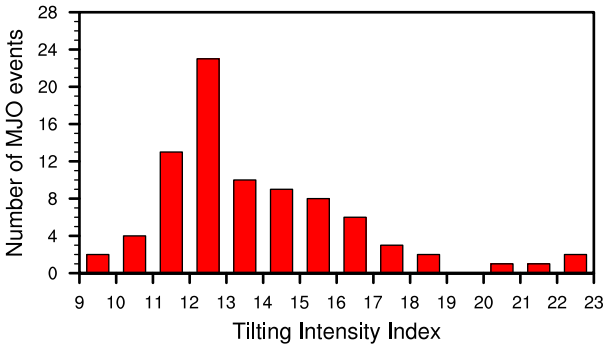

FIG. 2. Number of MJO events as a function of the tilting intensity index (unit: degrees in longitude).

each term on the rhs of Eq. (1) to the PBL moistening. Through this diagnosis, one may reveal specific physical processes through which the VTS affects the phase speed. It is worth noting a parallel calculation was done for different PBL depth (i.e., 1000–850 hPa). The comparison of the two results shows no significant difference, indicating that the results are not sensitive to the PBL depth (figures not shown).

e. Moist static energy budget diagnosis

To reveal the effect of the VTS on MJO phase speed from the second type of the moisture mode theory perspective, we conduct the MSE budget diagnosis. The MSE is defined as $m = C_pT + gz + Lq$, where T is temperature, z is height, C_p is the specific heat at constant pressure ($1004\,\mathrm{J\,K^{-1}\,kg^{-1}}$), and g is gravity acceleration ($9.8\,\mathrm{m\,s^{-2}}$). The column-integrated MSE budget equation on the intraseasonal time scale can be written as follows (Neelin and Held 1987; Wang et al. 2017):

$$\langle \partial_t m\rangle' = -\langle u\partial_x m\rangle' - \langle v\partial_y m\rangle' - \langle \omega\partial_p m\rangle' + Q'_R + Q'_t, \qquad (2)$$

where angle brackets denote a mass-weighted vertical integral from 1000 to 100 hPa. The first, second, and third terms in the rhs of Eq. (2) represent, respectively, zonal, meridional, and vertical MSE advection. The fourth term (Q_R) represents the sum of vertically integrated shortwave and longwave radiative heating rate, and the fifth term (Q_t) denotes the surface heat flux.

Given that MSE is a conservative quantity in the tropics in the absence of diabatic processes (Neelin and Held 1987) and that the MJO precipitation anomaly is in phase with the MSE anomaly (e.g., Jiang et al. 2015; Wang et al. 2017), it is desirable to analyze the relative contribution of the MSE budget terms on the rhs of Eq. (2) to the zonal asymmetry of the MSE tendency in order to understand the effect of the VTS on MJO eastward propagation.

3. Observed characteristics of the VTS and its relationship with phase speed

While the composite pattern shows a clear VTS (Fig. 1b), each of the individual MJO cases could differ. Figure 2 shows the tilting intensity index for each of 84 MJO events. Note that all the eastward propagating MJO events are accompanied by a VTS with a longitudinal distance ranging from 9° to 23°. The result seems to support the model diagnosis results by Wang et al. (2017), who found that the presence of a VTS is a key for separating the good and poor model groups in simulating MJO eastward propagation.

The average tilting intensity index for the 84 MJO events is 14.2° and the standard deviation is 2.7°. The standard deviation for 1281 samples (i.e., MJO days) is 4.5°. Based on the statistical characteristic, two groups of the MJO events are defined. One is the strong tilt group (STG; 15 events), defined as the tilting intensity index being greater than 0.7 standard deviations. The other is the weak tilt group (WTG; 19 events), defined as the tilting intensity index being less than −0.7 standard deviations.

Figure 3 shows the composite patterns of the vertical velocity and zonal wind fields for the two groups. The average tilting intensity index for the STG is 18.7°; it is 11.5° for the WTG. The difference can be clearly seen from the figure comparison. The descending motion to the east is stronger and close to MJO convective center in the STG, leading to a

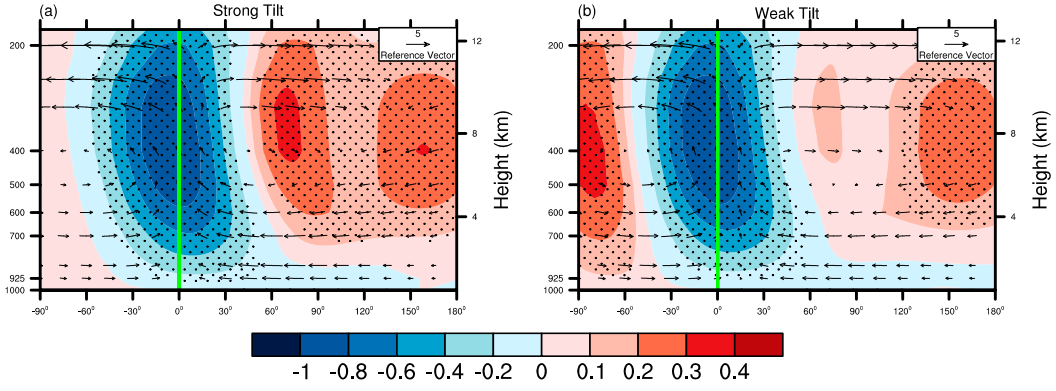

FIG. 3. Vertical–zonal cross sections of normalized anomalous vertical velocity (shaded) and zonal and vertical velocity (vectors; $\mathrm{m\,s^{-1}}$ for zonal wind and $0.02\,\mathrm{Pa\,s^{-1}}$ for vertical pressure velocity) fields averaged between 15° south and north relative to the MJO convective center, based on the (a) STG and (b) WTG composite. The green line denotes the MJO convective center. Areas with dots exceed a 95% confidence level with the Student's t test.

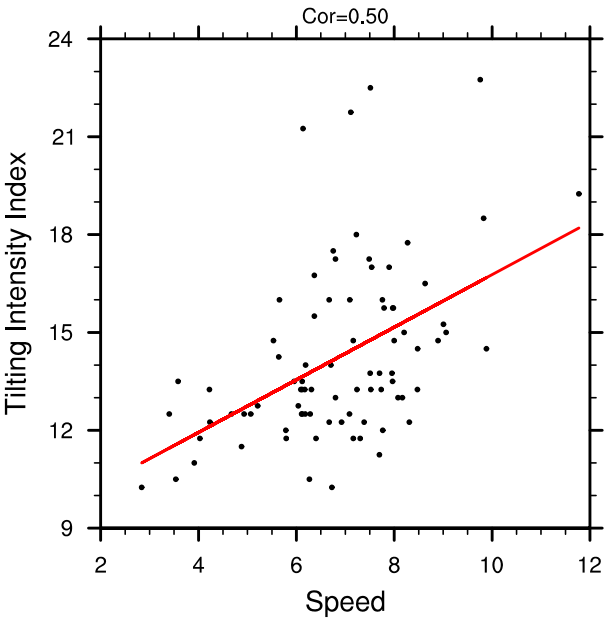

FIG. 4. Scatter diagram of the tilting intensity index (y axis; °) and the phase speed (x axis; m s^{-1}) for all 84 MJO events. The red line is the least squares fit line. The correlation coefficient is 0.50, exceeding the 99% confidence level with the Student's t test.

stronger vertical overturning circulation and a stronger easterly in the lower troposphere east of the MJO convection.

It is interesting to note that the average phase speed in the STG is 7.9 m s^{-1}, whereas for the WTG it is 5.9 m s^{-1}. The difference exceeds a 99% confidence level with the Student's t test. A stronger tilting is associated with a faster propagation speed. To further show that the VTS–phase speed relationship holds for all the MJO events, we plot the scatter diagram for all 84 MJO events (Fig. 4). The correlation coefficient between the tilting intensity index and phase speed is 0.5, exceeding a 99% confidence level with the Student's t test (the correlation coefficient of 0.28 corresponds to a 99% confidence level). This indicates that the VTS–phase speed relationship is statistically significant, and a stronger tilting structure corresponds to a faster eastward phase speed.

The observed VTS–phase speed relationship motivates us to further examine dynamic mechanisms behind the linkage. In the following section, we intend to reveal the dynamics behind the observed relationship from the two types of the moisture mode theory perspective.

4. Mechanisms responsible for the observed VTS–phase speed relationship

a. Understanding the impact of VTS on phase speed from the first type of moisture mode theory perspective

As discussed in the introduction section, the first type of the moisture mode theory emphasizes the zonal asymmetry of the perturbation moisture in the PBL (Hsu and Li 2012). A greater PBL moisture asymmetry would lead to a faster eastward phase speed. Figures 5a and 5b show the composite patterns of PBL moisture anomaly fields for the STG and WTG. While a positive moisture leading happens in both the groups, the amplitude of the moisture anomaly is greater in the STG than in the WTG, in particular over the key analysis domain (10°–40° in longitude, from −15° to 15° in latitude, relative to the MJO convective center).

Figure 5c further shows the relationship between the tilting intensity index and the PBL moisture anomaly averaged in the key analysis domain for all 84 MJO events. There is a significantly positive correlation between them. The correlation coefficient is 0.67, exceeding the 99% confident level with the Student's t test. This indicates that a stronger tilting structure corresponds to a stronger moisture leading.

According to the first type of the moisture mode theory, a stronger PBL moisture leading favors a greater phase speed. Figure 5d shows the scatter diagram for the domain averaged moisture anomaly and the phase speed for all the MJO events. The two variables are significantly positively correlated, indicating that a stronger moisture leading indeed leads to a faster eastward phase speed, consistent with the moisture mode theory.

What causes the difference of the PBL moisture anomaly between the STG and WTG? To address this question, a PBL averaged (1000–700 hPa) moisture budget analysis is conducted over the key analysis region (i.e., the black box in Fig. 5a). Figure 6 shows the budget analysis result. The largest contribution of the moisture leading in both groups arises from the vertical advection, followed by the meridional advection. The difference between STG and WTG is significantly positive, and is mainly controlled by the meridional and vertical advection (their differences exceed a 95% confidence level with the Student's t test). To reveal specific processes responsible for the moisture differences, the meridional and vertical advection terms are further separated into eight components, respectively, as follows:

$$-(v\partial_y q)' = -(\overline{v}\partial_y q')' - (\overline{v}\partial_y q^*)' - (v'\partial_y \overline{q})' - (v'\partial_y q')' - (v'\partial_y q^*)' - (v^*\partial_y \overline{q})' - (v^*\partial_y q')' - (v^*\partial_y q^*)', \tag{3}$$

$$-(\omega\partial_p q)' = -(\overline{\omega}\partial_p q')' - (\overline{\omega}\partial_p q^*)' - (\omega'\partial_p \overline{q})' - (\omega'\partial_p q')' - (\omega'\partial_p q^*)' - (\omega^*\partial_p \overline{q})' - (\omega^*\partial_p q')' - (\omega^*\partial_p q^*)', \tag{4}$$

where a prime denotes reconstructed variable representing the MJO-scale variable, a bar represents the background mean state (with a 100-day low-pass filtering), and an asterisk denotes a high-frequency variable (with a 20-day high-pass filtering). The diagnosis result shows (figures not shown) that the dominant terms are $-v'\partial_y\overline{q}$ (i.e., the advection of the mean moisture by anomalously MJO–time scale meridional wind) and $-\omega'\partial_p\overline{q}$ (i.e., the advection of the mean moisture by anomalously MJO–time scale vertical velocity).

Figure 7 shows the composite patterns of the anomalous circulation and the mean moisture fields averaged over the PBL for the STG and WTG. There are two Rossby gyres to the west of the MJO, induced by MJO convective heating, consistent with the Gill response. Induced by the descending

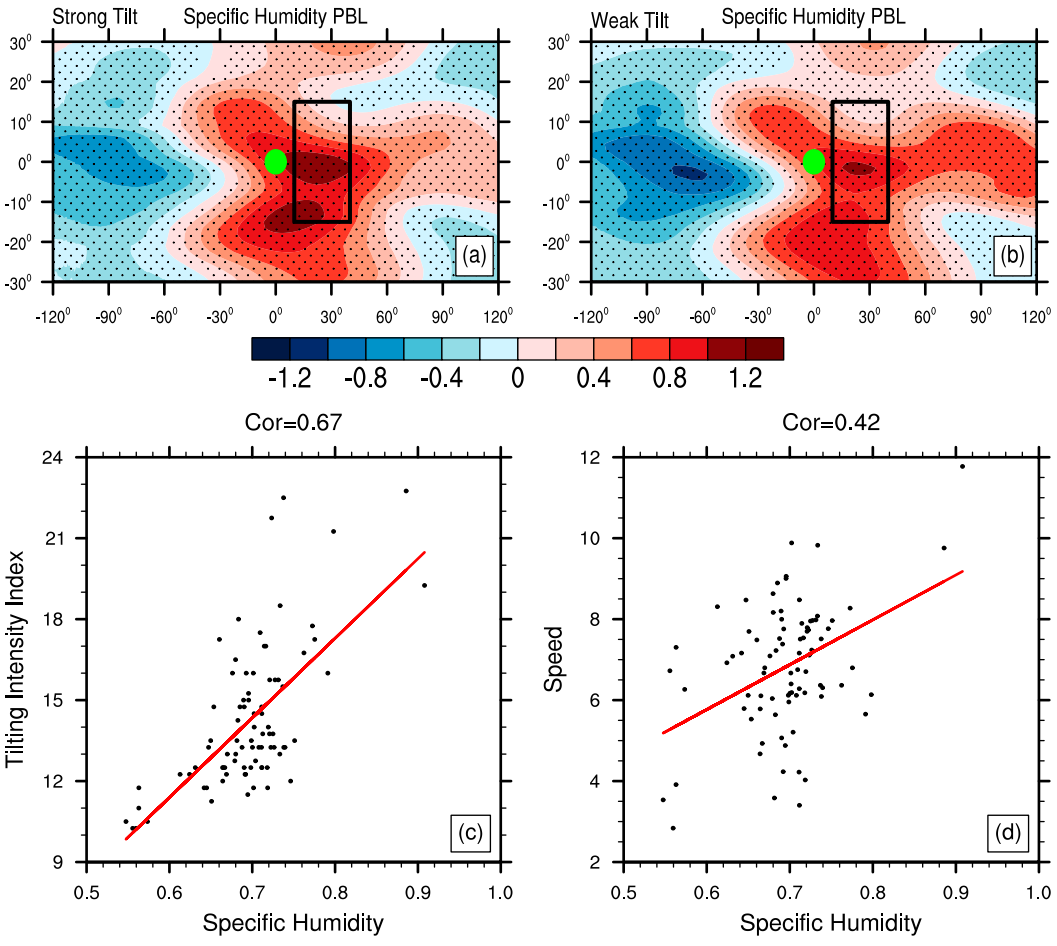

FIG. 5. (top) Composite patterns of normalized specific humidity anomaly (g kg^{-1}) averaged over the PBL (1000–700 hPa) based on the (a) STG and (b) WTG. The green dot denotes the MJO convective center. The black box represents a key analysis region. (bottom) Scatter diagrams of box-averaged specific humidity (x axis; g kg^{-1}) vs (c) the tilting intensity index (y axis; °) and (d) the phase speed (y axis; m s^{-1}) for all the MJO events. Correlation coefficients and least squares fit lines are shown at each panel.

motion to the east of MJO, there are also two Rossby gyres to the east, which is a little far away from the MJO convective center. The key region is occupied with anomalous poleward flow. Given the observed mean moisture distribution with a maximum near the equator, such a poleward flow would cause a positive meridional advection, resulting in a positive moisture leading.

Figure 7c shows that the difference of the anomalous circulation and the mean moisture between STG and WTG. To reveal their relative contributions to the anomalously meridional moisture advection, one may separate the advection difference term into the following four terms:

$$\Delta(-v'\partial_y\overline{q}) = -\Delta(\partial_y\overline{q})v' - \Delta(v')\partial_y\overline{q} - \Delta(\partial_y\overline{q})\Delta(v') + R, \quad (5)$$

where Δ denotes the difference between the STG and WTG (i.e., STG minus WTG); R represents the remaining item. The diagnosis result (Table 1) shows that the change of the anomalous wind is important, explaining about 67% of the change. The change of the mean moisture also plays a role, explaining about 33% of the change. The interaction between the change of anomalous wind and mean moisture can also explain 37% of the change. Therefore, it is both the enhanced poleward flow and the enhanced mean meridional moisture gradient that cause a greater positive meridional moisture advection anomaly in front of MJO convection in the STG.

Figure 8 shows the zonal–vertical sections of the anomalously vertical velocity and the mean moisture below 700 hPa. In the key analysis region, there is an ascending anomaly leading the MJO convective center in both the groups. As the mean moisture has a maximum at the surface and decays with height, an ascent anomaly results in a positive vertical advection anomaly. Using the same separation method as Eq. (5), the relative contribution of the anomalous wind and mean moisture changes can be assessed. Table 2 shows that the change of the anomalously vertical motion is important,

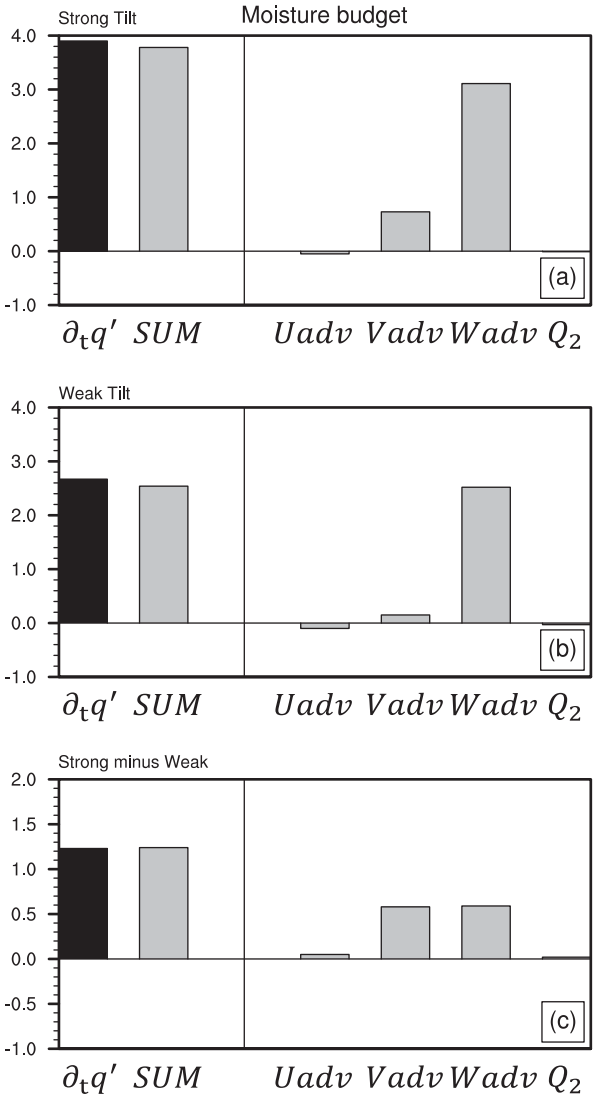

FIG. 6. PBL averaged (1000–700 hPa) moisture budget terms (10^{-7} kg m^{-2} s^{-1}) averaged over the key analysis region (i.e., the black box in Fig. 5a) for the (a) STG and (b) WTG, and (c) the difference between the STG and WTG. Bars from left to right represent, respectively, the specific humidity tendency, the sum of the budget terms in the right-hand side of Eq. (1), zonal advection, meridional advection, vertical advection, and condensational heating rate.

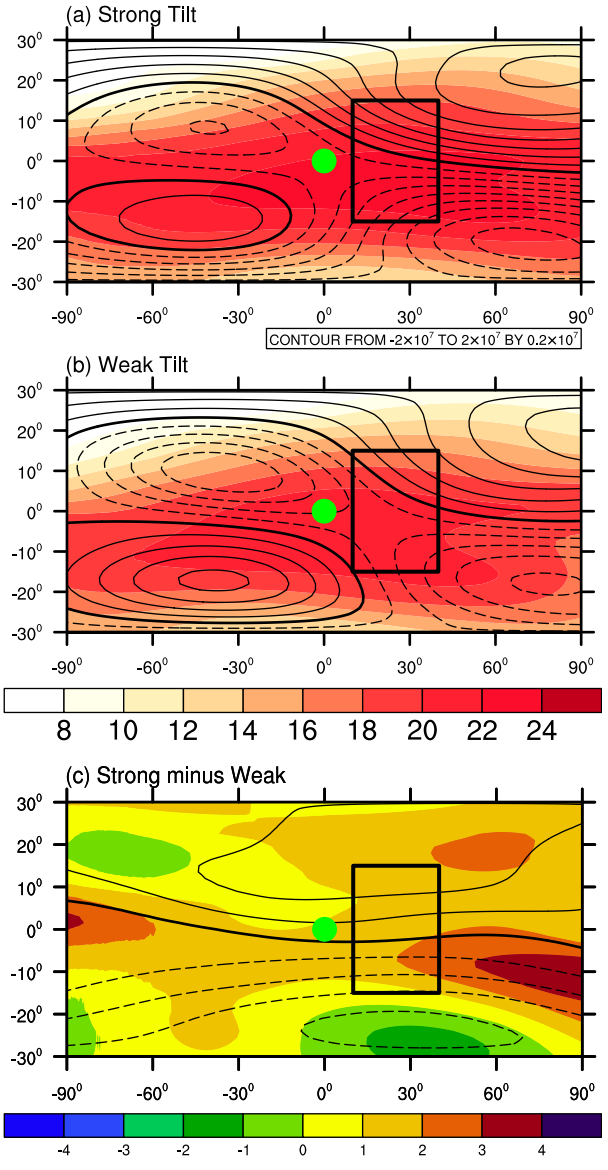

FIG. 7. Composite patterns of normalized streamfunction (vectors; m^2 s^{-1}) and the mean specific humidity (shaded; g kg^{-1}) fields averaged over the PBL (1000–700 hPa) based on the (a) STG and (b) WTG, and (c) their difference. The green dot denotes the MJO convective center. The black box denotes the key analysis region.

accounting for 125% of the vertical advection difference between STG and WTG. Figure 8c shows the difference fields. The increase of both the anomalous ascent and the mean moisture vertical gradient favors the enhanced vertical moisture advection in front of MJO convection in STG.

In summary, a greater PBL moisture anomaly is observed in front of MJO convection in the STG than in the WTG. The difference is primarily attributed to the increase of the anomalously poleward flow and ascending motion in the PBL, which result in stronger meridional and vertical moisture advection in the STG. This leads to a greater PBL moisture anomaly in front of MJO convection, favoring a faster phase speed.

TABLE 1. Relative contribution of the mean moisture and the anomalously meridional velocity to the difference of the anomalously meridional moisture advection between STG and WTG. Percentage of total change is in parentheses. Bold type denotes the most important item. Units are 10^{-7} kg m^{-2} s^{-1}.

$\Delta(-v'\partial_y\overline{q})$	$-\Delta(\partial_y\overline{q})v'$	$-\Delta(v')\partial_y\overline{q}$	$-\Delta(\partial_y\overline{q})\Delta(v')$	R
0.52	0.17 (33%)	**0.35 (67%)**	0.19 (37%)	−0.19

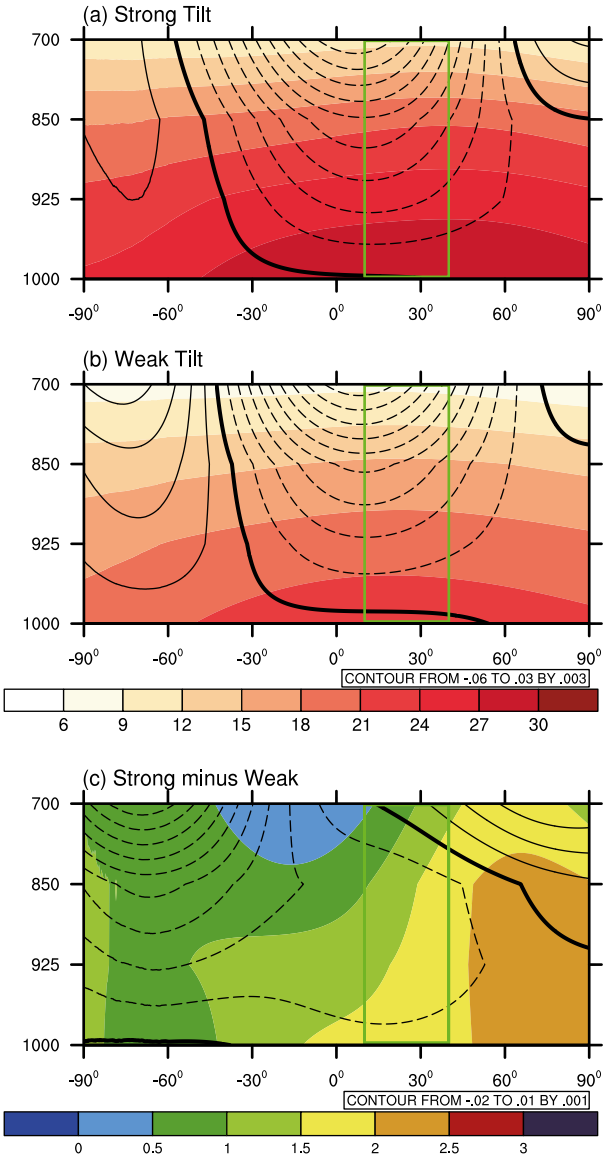

FIG. 8. Vertical–zonal cross sections of the anomalously vertical velocity (contours; Pa s^{-1}) and the mean specific humidity (shaded; g kg^{-1}) fields, averaged between 15° south and north relative to the MJO convective center, based on the (a) STG and (b) WTG, and (c) their difference. The green box denotes the key analysis region.

b. *Understanding the impact of VTS on phase speed from the second type of moisture mode theory perspective*

The second type of the moisture mode theory emphasizes the role of zonal asymmetry of the column-integrated MSE tendency on eastward propagation. Figure 9 shows the column-integrated MSE tendency patterns for the STG and WTG. Note that in both groups there are a positive MSE tendency to the east and negative tendency to the west of the MJO convective center, the gradient of which promotes the eastward propagation. The zonal gradient of the MSE tendency is stronger in the STG than in the WTG, which is consistent with a faster phase speed in STG.

TABLE 2. Relative contribution of the mean moisture and the anomalously vertical velocity to the difference of the anomalously vertical moisture advection between STG and WTG. Percentage of total change is in parentheses. Bold type denotes the most important item. Units are 10^{-7} kg m^{-2} s^{-1}.

$\Delta(-\omega'\partial_p\overline{q})$	$-\Delta(\partial_p\overline{q})\omega'$	$-\Delta(\omega')\partial_p\overline{q}$	$-\Delta(\partial_p\overline{q})\Delta(\omega')$	R
0.61	0.15 (26%)	**0.76 (125%)**	0.11 (18%)	−0.41

The two analysis boxes are selected to calculate the east–west gradient of the MSE tendency. The east box covers the region of 30°–120° in longitude and from −15° to 15° in latitude, relative to the MJO convective center, and the west box covers the region from −90° to 30° in relative longitude and from −15° to 15° in relative latitude. The reason why the domain over the east is larger than it over the west is that the positive MSE tendency to the east has a larger zonal extension than the negative anomaly to the west (Fig. 9) because the former corresponds to Kelvin wave response while the latter corresponds to Rossby wave response, which is consistent with Wang et al. (2018, 2020a). To cover both the Kelvin wave and Rossby wave effect, the domains are chosen to be larger to the east and smaller to the west. Figure 9c shows a scatter diagram for the tilting intensity index and the MSE tendency gradient (i.e., the east box minus the west box) for all the MJO cases. The correlation coefficient is 0.58, which indicates that there is a significantly positive relationship between the VTS and the MSE tendency gradient. A stronger tilting structure corresponds to a greater zonal asymmetry of the MSE tendency.

The relationship between the MSE tendency gradient and the phase speed is clearly revealed in Fig. 9d. They are significantly positively correlated, confirming that a stronger MSE tendency gradient indeed promotes a faster eastward phase speed.

What causes the distinctive MSE tendency gradient between the STG and WTG? To address this question, a column-integrated MSE budget analysis is conducted over the key analysis regions (i.e., the black boxes in Fig. 9a). Figure 10 shows the budget analysis result. The largest contribution of the east–west MSE tendency gradient in both groups comes from the meridional MSE advection, followed by the vertical advection. The difference between STG and WTG is positive and mainly controlled by the east region, while the west region plays the negative role in causing the difference of MSE tendency gradient. And the difference of MSE tendency gradient is primarily attributed to the vertical MSE advection. To reveal specific processes responsible for the difference, the vertical MSE advection is further separated into eight components as follows:

$$-\langle\omega\partial_p m\rangle' = -\langle\overline{\omega}\partial_p m'\rangle' - \langle\overline{\omega}\partial_p m^*\rangle' - \langle\omega'\partial_p\overline{m}\rangle' - \langle\omega'\partial_p m'\rangle' - \langle\omega'\partial_p m^*\rangle' - \langle\omega^*\partial_p m\rangle' - \langle\omega^*\partial_p m'\rangle' - \langle\omega^*\partial_p m^*\rangle'. \quad (6)$$

The result shows that $-\omega'\partial_p\overline{m}$ (i.e., the advection of the mean MSE by anomalously vertical motion) plays a key role.

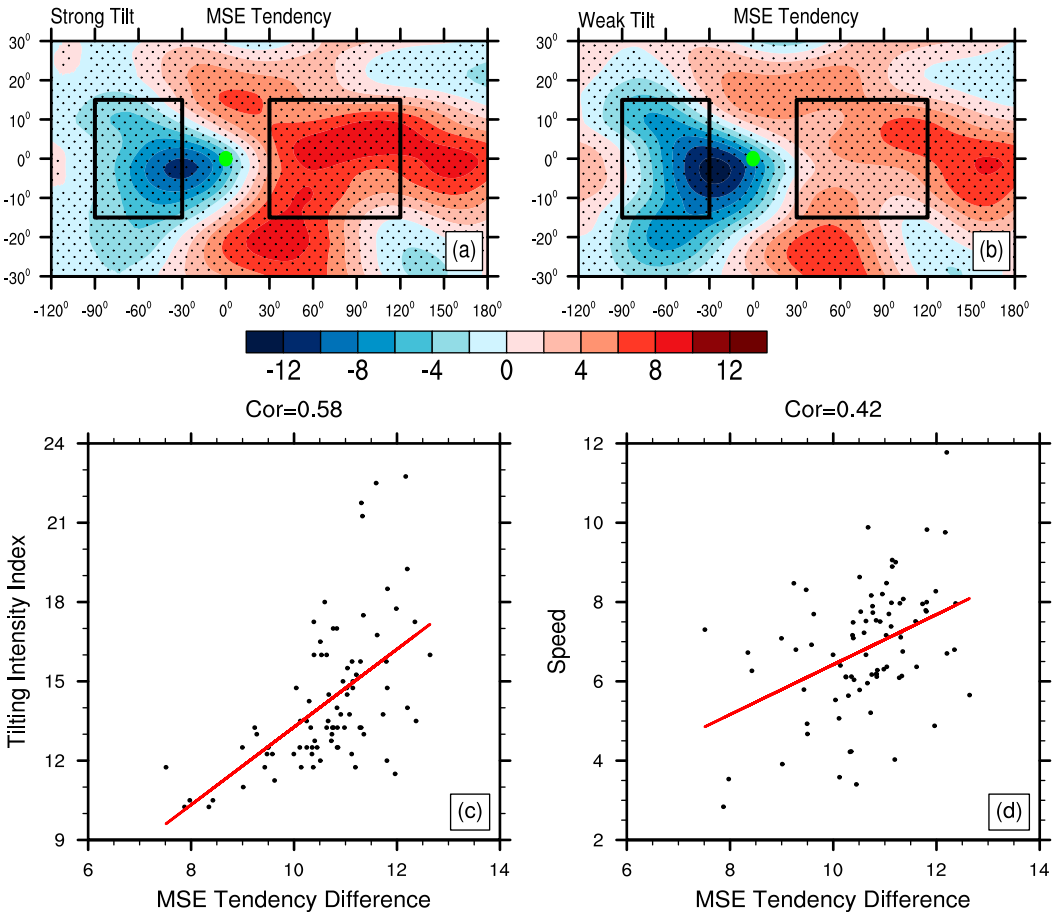

FIG. 9. (top) Composite patterns of the anomalous column-integrated MSE tendency (kg s^{-3}) based on the (a) STG and (b) WTG. The green dot denotes the MJO convective center. Black boxes represent the key analysis regions to represent the MSE tendency gradient. (bottom) Scatter diagrams of box averaged (east box minus west box) MSE tendency difference (x axis; kg s^{-3}) vs (c) the tilting intensity index (y axis; °) and (d) the phase speed (y axis; m s^{-1}) for all the 84 MJO events. Correlation coefficients and least squares fit lines are shown on each panel.

Figure 11 shows the zonal–vertical sections of the anomalously vertical velocity and mean MSE in the STG and WTG. Note that the mean MSE always has a minimum in middle troposphere (about 600 hPa) and a maximum near the tropopause and the surface. This is because the potential energy always increases with height while the mean temperature and humidity decrease with height. The anomalously vertical velocity field is characterized by a second-baroclinic-mode vertical structure away from the MJO deep convection region (Wang et al. 2017; Li and Hu 2019). There is anomalous descent in the upper troposphere and ascent at low levels in front of MJO convection. The vertical velocity is almost zero at the middle level. Such a vertical velocity profile leads to a positive vertical MSE advection anomaly to the east. The situation is just opposite to the west of the MJO convective center, with an ascent anomaly in the upper level and descent in the lower level. This feature is consistent with the VTS described in section 3. The zonal asymmetry of the MSE tendency promotes the eastward propagation of the MJO.

The difference of the anomalously vertical MSE advection between the STG and WTG may be decomposed into four terms as follows:

$$\Delta(-\omega'\partial_p\overline{m}) = -\Delta(\partial_p\overline{m})\omega' - \Delta(\omega')\partial_p\overline{m} - \Delta(\partial_p\overline{m})\Delta(\omega') + R\,. \tag{7}$$

Table 3 shows the diagnosis result. The difference of the anomalously vertical velocity plays an important role. Figure 11c shows the difference field. A positive (negative) difference appears to the east (west) of MJO, implying a strengthened vertical velocity anomaly in both the front and rear, and thus a greater MSE tendency asymmetry appears in the STG.

In summary, a greater MSE tendency asymmetry is observed in the STG than in the WTG. The strengthened tendency asymmetry results primarily from the advection of the mean MSE by anomalously vertical velocity. A strengthened upper-tropospheric descent (ascent) anomaly appears to the east (west) of MJO convection in the STG, leading to a

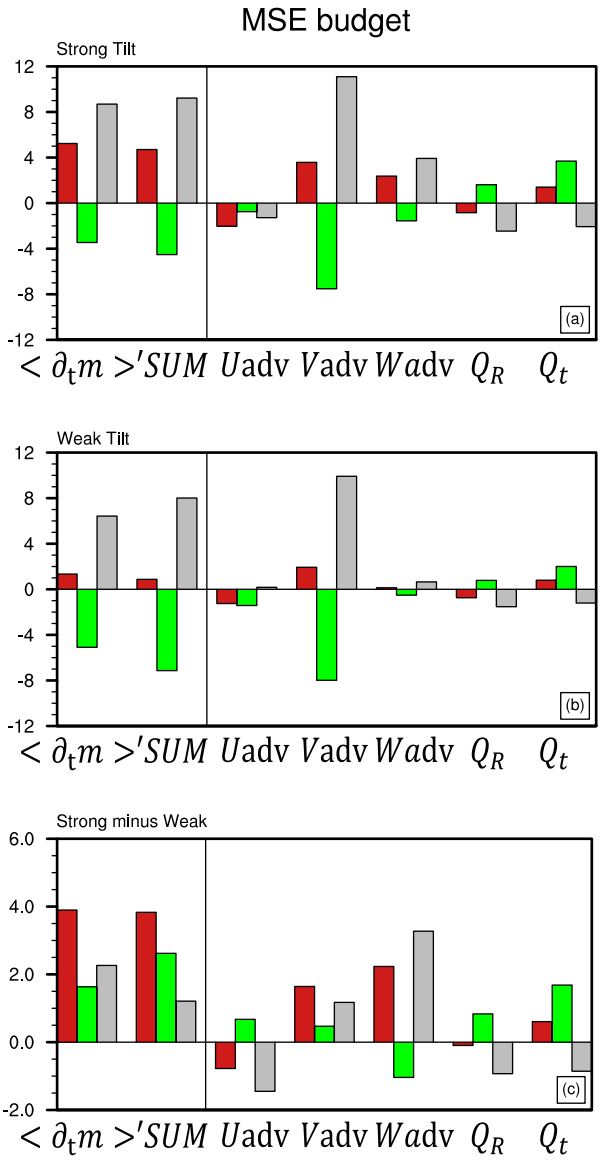

FIG. 10. Column-integrated MSE budget terms (kg s^{-3}) based on the (a) STG and (b) WTG, and (c) their difference. Bar groups from left to right represent, respectively, the MSE tendency, the sum of the budget terms in right-hand side of Eq. (2), zonal advection, meridional advection, vertical advection, radiation heating rate, and surface heat flux. Red, green, and gray bars represent, respectively, an average over the east box (from 30° to 120°, from −15° to 15°), the west box (from −90° to −30°, from −15° to 15°; black boxes in Fig. 9), and the east–west box difference.

stronger MSE tendency gradient and a faster eastward phase speed.

c. *Processes linking the VTS to the moisture/MSE tendency asymmetry*

The diagnosis above reveals a close link between the VTS and the PBL moisture asymmetry/MSE tendency asymmetry. It is primarily through the change of strength of the anomalous easterly at the low troposphere and sinking branch in front of MJO convection. The former influences the PBL moistening by affecting meridional and vertical moisture advection, whereas the latter affects the MSE tendency by influencing the vertical MSE advection. In this section, we further investigate possible processes through which the VTS influences the anomalous easterly and descent in front of MJO convection.

Through idealized numerical model experiments, Wang et al. (2017) showed that the occurrence of a tilted heating profile in the rear could cause a strengthened descent and a strengthened vertical overturning circulation in the front compared to a straight heating profile (see their Fig. 9). Figure 12a illustrates the relationship between the tilting intensity index and the free-atmospheric descending motion averaged over 200–700 hPa and 60°–90° in relative longitude (where the maximum sinking branch located). The correlation coefficient between them is 0.74, exceeding a 99% confidence level with the Student's *t* test. This indicates that a stronger tilting structure leads to a greater descent in the front, consistent with Wang et al. (2017). The stronger tilting structure, on the one hand, causes a greater negative vertical MSE advection to the west, and on the other hand it leads to a greater positive MSE tendency to the east of MJO convection (through enhancing the descent and vertical MSE advection). The stronger MSE tendency gradient promotes a faster phase speed, consistent with the second type of the moisture mode theory.

The enhanced overturning circulation in the front also strengthens the low-level easterly, promoting a stronger PBL convergence response. According to Hsu and Li (2012), the PBL convergence and ascending motion in front of MJO convection mainly result from the easterly anomaly and associated low pressure anomaly at the top of the PBL. Figure 12b shows the relationship between the descending motion in the front and the easterly anomaly at 700 hPa averaged over 10°–70° in relative longitude (which contains the range of easterly Kelvin wave response). The correlation coefficient is very high (−0.9), indicating a close connection.

Figure 12c is a scatter diagram between the anomalous easterly at the top of the PBL and the PBL divergence averaged over the key analysis region (i.e., the black box in Fig. 5a). The correlation coefficient between the two variables is 0.45, exceeding a 99% confidence level with the Student's *t* test. A stronger PBL convergence is associated with a stronger upward motion in the lower troposphere according to the mass continuity equation (the correlation coefficient between them is 0.99). The stronger ascent promotes a greater moisture anomaly through anomalously vertical advection, leading to a faster eastward phase speed.

A stronger descent in the front also results in a stronger low-level poleward flow through a Rossby wave response to a strengthened negative heating anomaly. Figure 12d shows the relationship between the anomalous descent and poleward flow. Here the equatorially antisymmetric component of the meridional velocity averaged over the key analysis region is used to measure the strength of the poleward flow. The correlation coefficient between them is 0.69, indicating their close relationship. It follows that a stronger poleward flow causes a

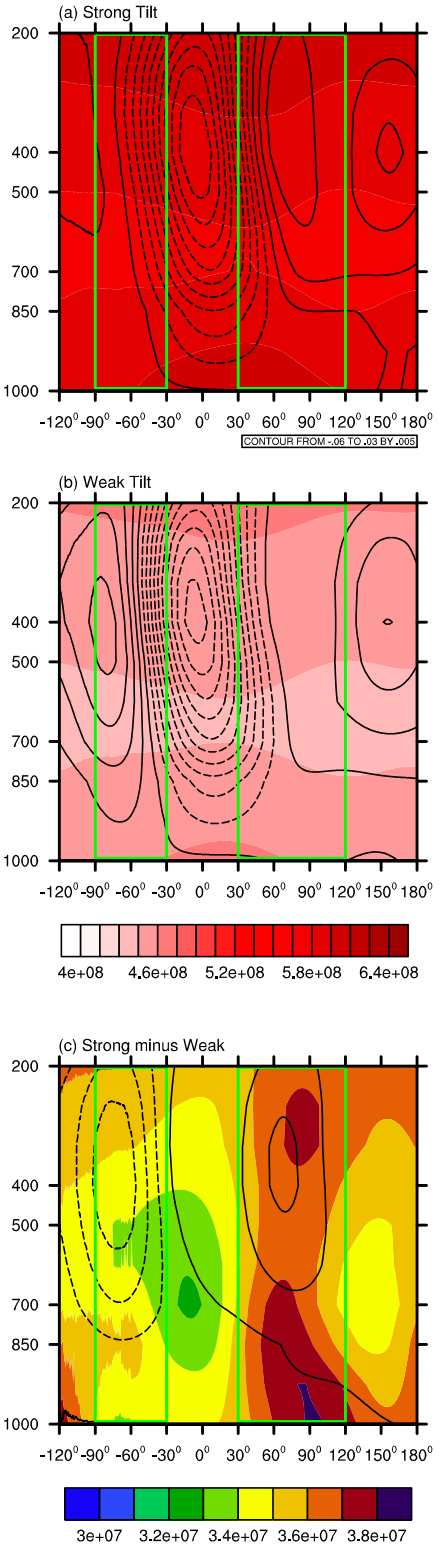

FIG. 11. Vertical–zonal cross sections of the anomalously vertical velocity (contour; Pa s^{-1}) and the mean MSE (shaded; $m^2 s^{-2}$) fields averaged between 15° south and north relative to the MJO convective center, based on the (a) STG and (b) WTG, and (c) their difference. Green boxes represent the key analysis regions.

stronger meridional moisture advection, leading to a stronger moisture anomaly in front of the convection and a faster phase speed.

d. Background conditions controlling the tilting strength

While the analysis above indicates a close linkage between the VTS and the phase speed, it is not clear what determines the tilting intensity. Figure 13 shows the background SST, PBL moisture, and equivalent potential temperature fields regressed onto the tilting intensity index for all the MJO events in fixed map to demonstrate the modulation of background signals on MJO tilting structure. It is worth mentioning that the mean MJO convective center (i.e., the green dot in Fig. 13) is the average location of 84 MJO events, as they all propagate from the tropical Indian Ocean to the tropical western Pacific. Here the background state represents the 100-day low-pass filtered variables. It is seen that over the tropical Indian Ocean where most of the MJO events were initiated, a warmer background SST and more humidity at the lower troposphere occur. Defining the background equivalent potential temperature difference between 500 and 200 hPa to represent the convective instability of the upper level (a positive difference implies a warmer potential temperature at 500 hPa), one may find that the upper troposphere is more convectively unstable when a stronger tilting structure is observed. Physically, one may argue that a warmer background SST, a greater column moisture, and a stronger upper-level convective instability favor the greater development of stratiform clouds to maintain the upper-level ascent in the rear of the MJO convection. This in turn promotes a more tilting vertical structure.

It is interesting to note that positive SST and moisture anomalies appear in the eastern Pacific, resembling an El Niño pattern, which is beneficial for a stronger MJO tilting. The finding that an El Niño pattern corresponds to faster propagation of MJO is consistent with Wang et al. (2019), who proposed that in the condition of an El Niño, the Indo-Pacific warm pool and the associated active convective region expand eastward, leading to an increased zonal scale and faster propagation of the MJO. However, the physical mechanism through which the eastern Pacific SST anomaly affects the MJO tilting structure remains unknown, and the discussion above is qualitative. Further in-depth observational and modeling studies are needed to understand the background impact.

5. Summary and discussion

The impact of vertically tilted structure on MJO phase propagation was found based on a previous model diagnosis study (Wang et al. 2017). It is not clear whether or not this tilting structure exists in the observational data, and if it does exist, what its relationship is with MJO phase speed. In this work, through a detailed diagnosis of the 33-yr observational data, we intend to address these two scientific questions.

The MV-EOF is used to isolate the eastward propagating MJO signal. A total of 84 MJO events are selected for the 33 northern winter seasons. It is interesting to note that all the MJO events are accompanied with vertically tilted structure, ranging from 9° to 23°. The average and standard deviation are

TABLE 3. Relative contribution of the mean MSE and the anomalously vertical velocity to the difference of the anomalously vertical MSE advection between STG and WTG. Percentage of total change is in parentheses. Bold type denotes the most important item. Units are kg s^{-3}.

$\Delta(-\omega'\partial_p\overline{m})$	$-\Delta(\partial_p\overline{m})\omega'$	$-\Delta(\omega')\partial_p\overline{m}$	$-\Delta(\partial_p\overline{m})\Delta(\omega')$	R
3.01	−0.88 (29%)	**6.22 (207%)**	0.02 (1%)	−2.35

14.2° and 2.7°, respectively. A composite is done for the strong and weak tilt groups. It is found that the average phase speeds of the two groups are significantly different, with 7.9 m s^{-1} for STG and 5.9 m s^{-1} for WTG. The VTS–phase speed relationship is further confirmed by individual MJO events, with a correlation coefficient of 0.50, exceeding a 99% confidence level with the Student's t test.

The impact of the VTS on the phase speed is investigated from two types of the moisture model theory perspectives. The physical mechanism is shown in Fig. 14. The first type of the moisture mode theory emphasizes the moisture asymmetry in the PBL. It was shown that a positive PBL moisture anomaly in front of the convection could trigger the local convective instability and promote the eastward propagation (Hsu and Li 2012; Chen and Wang 2020). While both the STG and WTG present a positive PBL moisture leading, a stronger tilting leads to a greater perturbation moisture in the front through enhanced vertical and meridional moisture advection (according to a moisture budget analysis).

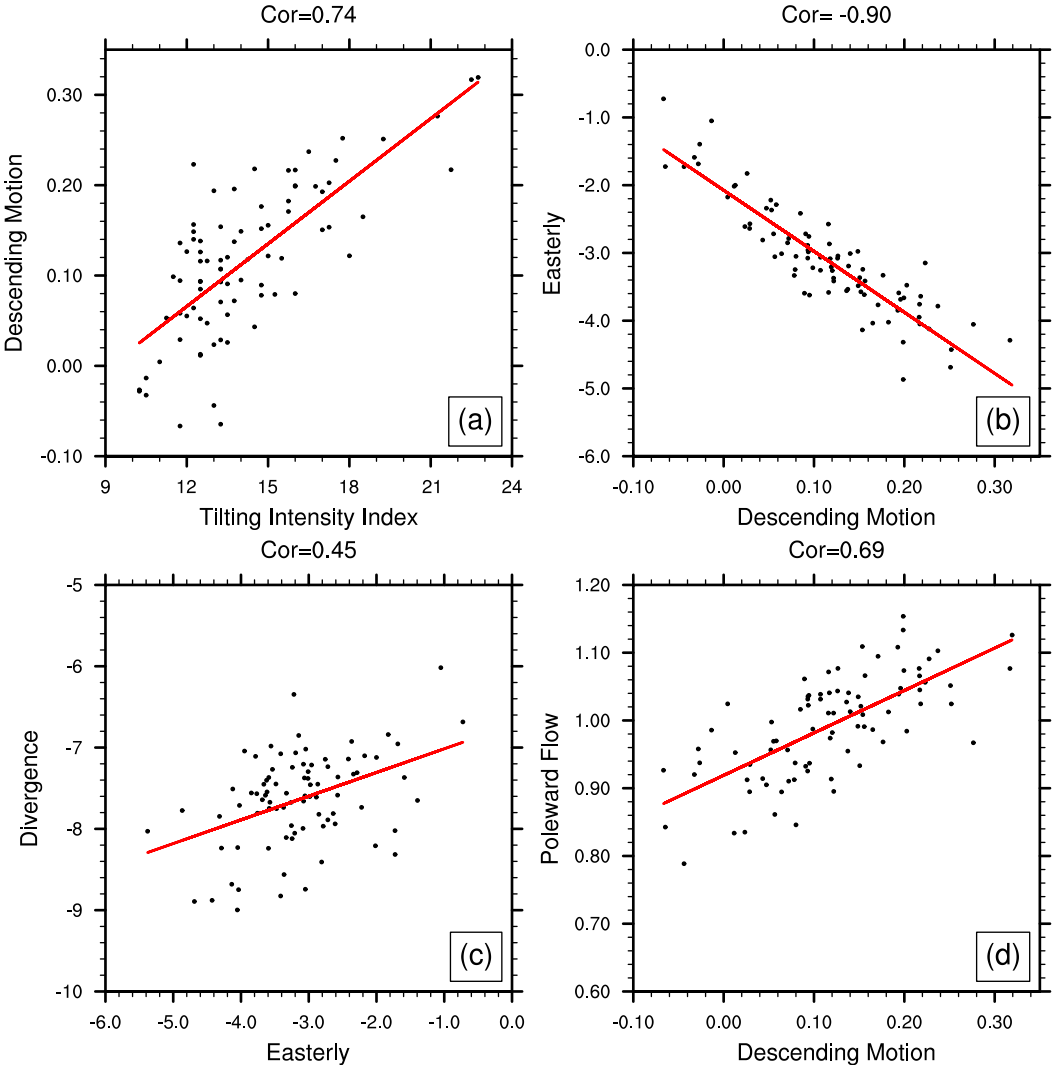

FIG. 12. Scatterplots of (a) the tilting intensity index (x axis; °) vs the anomalous descent in front of the MJO convection (y axis; 200–700 hPa, 60°–90° in relative longitude; Pa s^{-1}), (b) the anomalous descent [as in (a); x axis; Pa s^{-1})] vs the easterly anomaly at 700 hPa averaged over 10°–70° in relative longitude (y axis; m s^{-1}), (c) the easterly anomaly [as in (b); x axis; m s^{-1}] vs PBL (1000–700 hPa) divergence averaged over 10°–40° in relative longitude (y axis; m s^{-1}), and (d) the anomalous descent [as in (a); x axis; Pa s^{-1}] vs the poleward flow anomaly at 700 hPa averaged over 10°–40° in relative longitude (y axis; m s^{-1}). Correlation coefficients and least squares fit lines are shown on each panel.

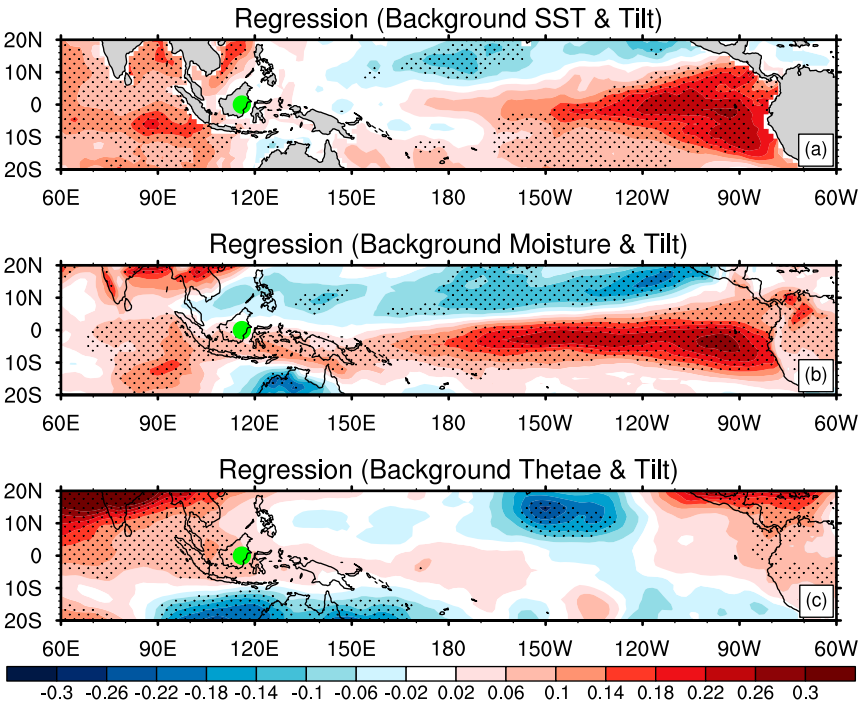

FIG. 13. Regressed fields of (a) background SST (°C), (b) moisture averaged over the PBL (g kg^{-1}), and (c) the difference of equivalent potential temperature between 500 and 200 hPa (K) onto MJO tilting intensity index. The green dot denotes mean MJO convective center position (116°E). Areas with dots exceed a 95% confidence level with the Student's *t* test.

It is found that a stronger tilting in the rear leads to a greater descent in the front. The two variables are significantly correlated (with a high correlation coefficient of 0.74) for all the 84 MJO events. The observed relationship is supported by the idealized numerical model experiments of Wang et al. (2017), who found that a backward tilting heating would cause a stronger descent to the east. The stronger descent may further cause a negative heating in situ, which induces a stronger poleward flow and a stronger easterly response to its west, as a Rossby wave response (Gill 1980). On the one hand, the enhanced poleward flow results in a greater meridional moisture advection. On the other hand, the stronger easterly response at the top of the PBL leads to a greater convergence (Hsu and Li 2012) and greater ascent in the PBL, which results in a greater vertical moisture advection. Both the processes lead to a greater PBL moisture in front of the convection and thus a faster phase speed as shown in Fig. 14.

The second type of the moisture mode theory emphasizes the column-integrated MSE tendency asymmetry. It has been shown that the MSE center is approximately in phase with the MJO convective center (Jiang et al. 2015; Wang et al. 2017). A zonally asymmetric MSE tendency with a positive tendency to the east and a negative tendency to the west could promote the eastward propagation of the MJO. Under this theoretical framework, whether or not the PBL moisture itself is asymmetric is not critical. It is found that a greater tilting leads to a greater column integrated MSE tendency gradient. A MSE budget analysis shows that the cause of this relationship lies on the anomalously vertical MSE advection in the upper troposphere, especially the positive advection to the east. A stronger tilting in the rear causes a greater descent anomaly to the east of the MJO convection. Such a vertical velocity distribution leads to a positive (negative) MSE vertical advection anomaly to the east (west), given the observed mean MSE vertical profile. This strengthens the zonal gradient of the MSE tendency and promotes faster eastward propagation as shown in Fig. 14.

It is found that the vertical tilting intensity is modulated by the background state. To the west of the MJO center, the background SST, low-level specific humidity, and upper-tropospheric convective instability (represented by the difference of equivalent potential temperature between 500 and 200 hPa) appear greater when the tilting is greater. Besides, the eastern Pacific Ocean is occupied by warm SST and positive moisture, just like an El Niño pattern. This indicates that the background state plays an important role in modulating the MJO tilting structure.

It is worth noting that MJO amplitude is not considered in the current work. All variables have been normalized, which represents the comparison is done based on the same MJO strength. The correlation coefficient between MJO amplitude and phase speed is −0.06, which denotes there is no direct relationship between them. Note that there are many studies focusing on the vertical tilting structure at the east of MJO convection, particularly PBL ascent leading; the emphasis of our paper is on the tilting structure in the rear of the MJO. A similar tilting intensity index is defined to the east of the MJO. The correlation coefficient between tilting intensity index in

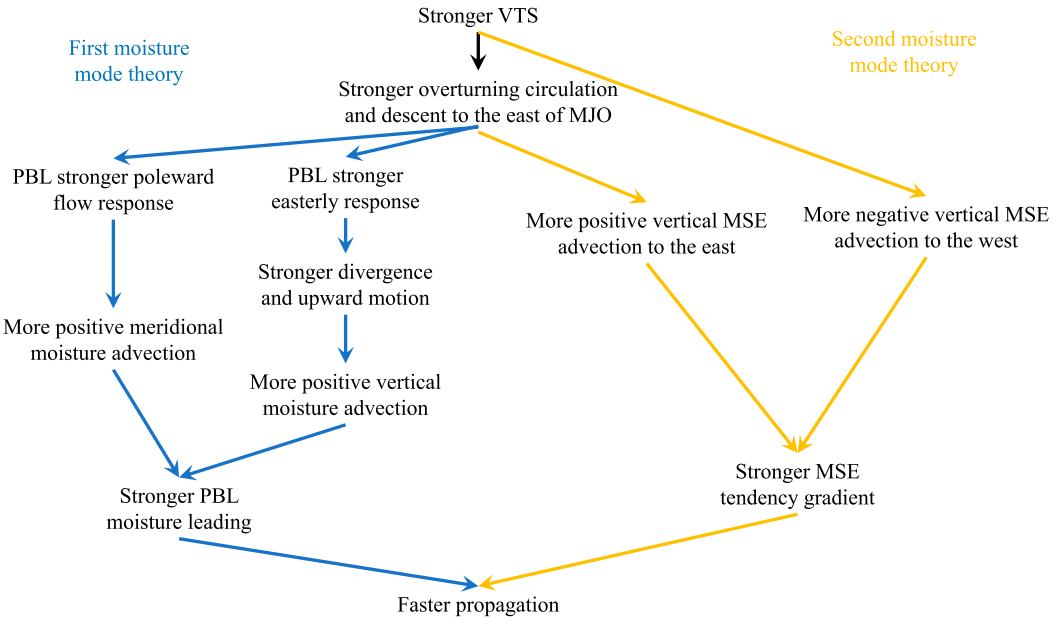

FIG. 14. Schematic diagram illustrating the positive relationship between VTS and MJO phase speed from the perspective of the first moisture mode theory (PBL moisture leading; blue arrows) and the second moisture mode theory (MSE tendency asymmetry; yellow arrows).

the front and in the rear is almost zero, which denotes that there is no direct connection between the tilted structure in the front and the rear. Besides, the relationship between the tilting intensity index in the front and MJO phase speed is not significant (correlation coefficient is 0.1). Kerns and Chen (2014, 2015) proposed that dry air advection from the subtropics to tropics favored the initiation and eastward propagation of MJO by suppressing the convection on the west side of MJO, which required more observational proof and further in-depth research. Thus, we analyze the zonal gradient of PBL moisture. Results show that there is no significant relationship between it and the MJO phase speed (the correlation coefficient is −0.24).

While the current diagnoses are based on the two types of moisture mode theories, it is worth mentioning that a number of MJO theories have been developed during the past decades [see recent review papers by Zhang et al. (2020) and Jiang et al. (2020)]. Early theoretical studies regarded the MJO as a moist Kelvin wave modified by convective heating through a wave-CISK (conditional instability of the second kind) mechanism (e.g., Lau and Peng 1987; Chang and Lim 1988), a wind-induced surface heat exchange (WISHE) mode (Emanuel 1987), or a convection–frictional convergence (CFC) feedback mode (Wang and Rui 1990; Wang and Li 1994; Li and Wang 1994). More recently, a skeleton theory (e.g., Majda and Stechmann 2009; Thual et al. 2014; Thual and Majda 2015, 2016) and a gravity wave interference theory (Yang and Ingersoll 2013, 2014) were proposed. It is desirable to validate the current VTS–phase speed relationship from the aforementioned different theoretical frameworks.

It is worth mentioning that the average phase speed of each MJO event in the current work is calculated based on the slope of a least squares fit line of the MJO convective centers. Such a method might overestimate the MJO propagation speed and ignore some propagation features, such as that the MJO often slows down in the MC and propagates faster in colder sea surface. To clearly describe the overestimating extent, another method is applied to calculate the MJO phase speed by using the center difference of the longitude of the MJO convective center to represent each day's propagation speed. The phase speed for a MJO event is the average during the MJO life cycles. On this basis, the average is 5.3 m s^{-1}, a reduction of about 22% from the original method in the paper (the average speed is 6.8 m s^{-1} based on the slope of a least squares fit line). Although the phase speed varies in difference method, the positive relationship between MJO phase speed and vertical tilted structure is robust. Other methods such as those proposed by Zhang and Ling (2017) and Chen and Wang (2020), who found a tracking line to describe the eastward propagation of MJO in the time–longitude section, may also be used for comparison. Further in-depth studies are needed to resolve these open issues.

Acknowledgments. This work was jointly supported by NSFC Grants 42088101 and 41875069, NOAA NA18OAR4310298, NSF AGS-1643297, the China Scholarship Council (CSC) under N201908320493, and the Postgraduate Research and Practice Innovation Program of Jiangsu Province KYCX19_1014 and KYCX19_1023. This is SOEST contribution number 11312, IPRC contribution number 1516, and ESMC number 347.

Data availability statement. Datasets are available in a public repository that assigns persistent identifiers to datasets.
1) Daily outgoing longwave radiation (OLR) data used during this study are openly available from the National Oceanic and Atmospheric Administration (NOAA) at https://psl.noaa.gov/

data/gridded/data.interp_OLR.html as cited in Liebmann and Smith (1996).

2) Daily reanalysis data consist of three-dimensional wind, geopotential height, temperature, specific humidity, and surface heat fluxes fields are openly available from the European Center for Medium-Range Weather Forecasts interim reanalysis (ERA-I) at https://rda.ucar.edu/datasets/ds627.0/ as cited in Dee et al. (2011).

REFERENCES

Adames, Á. F., and D. Kim, 2016: The MJO as a dispersive, convectively coupled moisture wave: Theory and observations. *J. Atmos. Sci.*, **73**, 913–941, https://doi.org/10.1175/JAS-D-15-0170.1.

Andersen, J. A., and Z. Kuang, 2012: Moist static energy budget of MJO-like disturbances in the atmosphere of a zonally symmetric aquaplanet. *J. Climate*, **25**, 2782–2804, https://doi.org/10.1175/JCLI-D-11-00168.1.

Benedict, J. J., and D. A. Randall, 2007: Observed characteristics of the MJO relative to maximum rainfall. *J. Atmos. Sci.*, **64**, 2332–2354, https://doi.org/10.1175/JAS3968.1.

Chang, C. P., and H. Lim, 1988: Kelvin wave-CISK: A possible mechanism for the 30–50 day oscillations. *J. Atmos. Sci.*, **45**, 1709–1720, https://doi.org/10.1175/1520-0469(1988)045<1709:KWCAPM>2.0.CO;2.

Chen, G., and B. Wang, 2020: Circulation factors determining the propagation speed of the Madden–Julian oscillation. *J. Climate*, **33**, 3367–3380, https://doi.org/10.1175/JCLI-D-19-0661.1.

Dee, D. P., and Coauthors, 2011: The ERA-Interim reanalysis: Configuration and performance of the data assimilation system. *Quart. J. Roy. Meteor. Soc.*, **137**, 553–597, https://doi.org/10.1002/qj.828.

Del Genio, A. D., Y. Chen, D. Kim, and M.-S. Yao, 2012: The MJO transition from shallow to deep convection in CloudSat/CALIPSO data and GISS GCM simulations. *J. Climate*, **25**, 3755–3770, https://doi.org/10.1175/JCLI-D-11-00384.1.

Emanuel, K. A., 1987: An air–sea interaction model of intraseasonal oscillations in the tropics. *J. Atmos. Sci.*, **44**, 2324–2340, https://doi.org/10.1175/1520-0469(1987)044<2324:AASIMO>2.0.CO;2.

Feng, J., T. Li, and W. Zhu, 2015: Propagating and non-propagating MJO events over the Maritime Continent. *J. Climate*, **28**, 8430–8449, https://doi.org/10.1175/JCLI-D-15-0085.1.

Fu, X., and B. Wang, 2009: Critical roles of the stratiform rainfall in sustaining the Madden–Julian oscillation: GCM experiments. *J. Climate*, **22**, 3939–3959, https://doi.org/10.1175/2009JCLI2610.1.

Gill, A. E., 1980: Some simple solutions for heat-induced tropical circulation. *Quart. J. Roy. Meteor. Soc.*, **106**, 447–462, https://doi.org/10.1002/qj.49710644905.

Hendon, H. H., and M. L. Salby, 1994: The life cycle of the Madden–Julian oscillation. *J. Atmos. Sci.*, **51**, 2225–2237, https://doi.org/10.1175/1520-0469(1994)051<2225:TLCOTM>2.0.CO;2.

Hsu, P.-C., and T. Li, 2012: Role of the boundary layer moisture asymmetry in causing the eastward propagation of the Madden–Julian oscillation. *J. Climate*, **25**, 4914–4931, https://doi.org/10.1175/JCLI-D-11-00310.1.

Hu, F., and Coauthors, 2020: Reexamining the moisture mode theories of the Madden–Julian oscillation based on observational analyses. *J. Climate*, **34**, 839–853, https://doi.org/10.1175/JCLI-D-20-0441.1.

Jiang, X., and Coauthors, 2015: Vertical structure and physical processes of the Madden–Julian oscillation: Exploring key model physics in climate simulations. *J. Geophys. Res. Atmos.*, **120**, 4718–4748, https://doi.org/10.1002/2014JD022375.

——, and Coauthors, 2020: Fifty years of research on the Madden–Julian Oscillation: Recent progress, challenges, and perspectives. *J. Geophys. Res. Atmos.*, **125**, e2019JD030911, https://doi.org/10.1029/2019JD030911.

Johnson, R. H., and P. E. Ciesielski, 2013: Structure and properties of Madden–Julian oscillations deduced from DYNAMO sounding arrays. *J. Atmos. Sci.*, **70**, 3157–3179, https://doi.org/10.1175/JAS-D-13-065.1.

——, T. M. Rickenbach, S. A. Rutledge, P. E. Ciesielski, and W. H. Schubert, 1999: Trimodal characteristics of tropical convection. *J. Climate*, **12**, 2397–2418, https://doi.org/10.1175/1520-0442(1999)012<2397:TCOTC>2.0.CO;2.

Kerns, B. W., and S. S. Chen, 2014: Equatorial dry air intrusion and related synoptic variability in MJO initiation during DYNAMO. *Mon. Wea. Rev.*, **142**, 1326–1343, https://doi.org/10.1175/MWR-D-13-00159.1.

——, and ——, 2015: ECMWF and GFS model forecast verification during DYNAMO: Multiscale variability in MJO initiation over the equatorial Indian Ocean. *J. Geophys. Res. Atmos.*, **119**, 3736–3755, https://doi.org/10.1002/2013JD020833.

Khouider, B., and A. J. Majda, 2008: Multicloud models for organized tropical convection: Enhanced congestus heating. *J. Atmos. Sci.*, **65**, 895–914, https://doi.org/10.1175/2007JAS2408.1.

Kikuchi, K., and Y. N. Takayabu, 2004: The development of organized convection associated with the MJO during TOGA COARE IOP: Trimodal characteristics. *Geophys. Res. Lett.*, **31**, L10101, https://doi.org/10.1029/2004GL019601.

Kiladis, G. N., M. C. Wheeler, P. T. Haertel, K. H. Straub, and P. E. Roundy, 2009: Convectively coupled equatorial waves. *Rev. Geophys.*, **47**, RG2003, https://doi.org/10.1029/2008RG000266.

Kim, D., and E. D. Maloney, 2017: Simulation of the Madden–Julian oscillation using general circulation models. *The Global Monsoon System: Research and Forecast*, C.-P. Chang et al., Eds., World Scientific, 119–130.

——, J. S. Kug, and A. H. Sobel, 2014: Propagating versus nonpropagating Madden–Julian oscillation events. *J. Climate*, **27**, 111–125, https://doi.org/10.1175/JCLI-D-13-00084.1.

Knutson, T. R., K. M. Weickmann, and J. E. Kutzbach, 1986: Global-scale intraseasonal oscillations of outgoing longwave radiation and 250 mb zonal wind during Northern Hemisphere summer. *Mon. Wea. Rev.*, **114**, 605–623, https://doi.org/10.1175/1520-0493(1986)114<0605:GSIOOO>2.0.CO;2.

Lau, K.-M., and P. H. Chan, 1986: Aspects of the 40–50 day oscillation during the northern summer as inferred from outgoing longwave radiation. *Mon. Wea. Rev.*, **114**, 1354–1367, https://doi.org/10.1175/1520-0493(1986)114<1354:AOTDOD>2.0.CO;2.

——, and L. Peng, 1987: Origin of low-frequency (intraseasonal) oscillations in the tropical atmosphere. Part I: Basic theory. *J. Atmos. Sci.*, **44**, 950–972, https://doi.org/10.1175/1520-0469(1987)044<0950:OOLFOI>2.0.CO;2.

Lau, N.-C., and K.-M. Lau, 2010: The structure and propagation of intraseasonal oscillations appearing in a GFDL general circulation model. *J. Atmos. Sci.*, **43**, 2023–2047, https://doi.org/10.1175/1520-0469(1986)043<2023:TSAPOI>2.0.CO;2.

Li, T., 2014: Recent advance in understanding the dynamics of the Madden–Julian oscillation. *J. Meteor. Res.*, **28** (1), 1–33, https://doi.org/10.1007/s13351-014-3087-6.

——, and B. Wang, 1994: The influence of sea surface temperature on the tropical intraseasonal oscillation: A numerical study. *Mon. Wea. Rev.*, **122**, 2349–2362, https://doi.org/10.1175/1520-0493(1994)122<2349:TIOSST>2.0.CO;2.

——, and C. Zhou, 2009: Planetary scale selection of the Madden–Julian oscillation. *J. Atmos. Sci.*, **66**, 2429–2443, https://doi.org/10.1175/2009JAS2968.1.

——, and P.-C. Hsu, 2017: *Fundamentals of Tropical Climate Dynamics*. Springer, 229 pp.

——, and F. Hu, 2019: A coupled moisture–dynamics model of the Madden–Julian oscillation: Convection interaction with first and second baroclinic modes and planetary boundary layer. *Climate Dyn.*, **53**, 5529–5546, https://doi.org/10.1007/s00382-019-04879-x.

——, J. Ling, and P. Hsu, 2020: Madden–Julian oscillation: Its discovery, dynamics, and impact on East Asia. *J. Meteor. Res.*, **34**, 20–42, https://doi.org/10.1007/s13351-020-9153-3.

Liebmann, B., and C. A. Smith, 1996: Description of a complete (interpolated) outgoing longwave radiation dataset. *Bull. Amer. Meteor. Soc.*, **77**, 1275–1277, https://doi.org/10.1175/1520-0477-77.6.1274 (associated data available at https://psl.noaa.gov/data/gridded/data.interp_OLR.html).

Liu, F., and B. Wang, 2017: Effects of moisture feedback in a frictional coupled Kelvin–Rossby wave model and implication in the Madden–Julian oscillation dynamics. *Climate Dyn.*, **48**, 513–522, https://doi.org/10.1175/JCLI-D-17-0003.1.

Madden, R. A., and P. R. Julian, 1971: Detection of a 40–50 day oscillation in the zonal wind in the tropical Pacific. *J. Atmos. Sci.*, **28**, 702–708, https://doi.org/10.1175/1520-0469(1971)028<0702:DOADOI>2.0.CO;2.

——, and ——, 1972: Description of global-scale circulation cells in the tropics with a 40–50 day period. *J. Atmos. Sci.*, **29**, 1109–1123, https://doi.org/10.1175/1520-0469(1972)029<1109:DOGSCC>2.0.CO;2.

Majda, A. J., and S. N. Stechmann, 2009: The skeleton of tropical intraseasonal oscillations. *Proc. Natl. Acad. Sci. USA*, **106**, 8417–8422, https://doi.org/10.1073/pnas.0903367106.

Maloney, E. D., 2009: The moist static energy budget of a composite tropical intraseasonal oscillation in a climate model. *J. Climate*, **22**, 711–729, https://doi.org/10.1175/2008JCLI2542.1.

——, Á. F. Adames, and H. X. Bui, 2019: Madden–Julian oscillation changes under anthropogenic warming. *Nat. Climate Change*, **9**, 26–33, https://doi.org/10.1038/s41558-018-0331-6.

Mapes, B. E., 2000: Convective inhibition, subgrid-scale triggering energy, and stratiform instability in a toy tropical wave model. *J. Atmos. Sci.*, **57**, 1515–1535, https://doi.org/10.1175/1520-0469(2000)057<1515:CISSTE>2.0.CO;2.

Neelin, J. D., and I. M. Held, 1987: Modeling tropical convergence based on the moist static energy budget. *Mon. Wea. Rev.*, **115**, 3–12, https://doi.org/10.1175/1520-0493(1987)115<0003:MTCBOT>2.0.CO;2.

Ren, P., H.-L. Ren, J.-X. Fu, J. Wu, L. Du, 2018: Impact of boreal summer intraseasonal oscillation on rainfall extremes in southeastern China and its predictability in CFSv2. *J. Geophys. Res. Atmos.*, **123**, 4423–4442, https://doi.org/10.1029/2017JD028043.

Sobel, A., and E. Maloney, 2012: An idealized semi-empirical framework for modeling the Madden–Julian oscillation. *J. Atmos. Sci.*, **69**, 1691–1705, https://doi.org/10.1175/JAS-D-11-0118.1.

——, and ——, 2013: Moisture modes and the eastward propagation of the MJO. *J. Atmos. Sci.*, **70**, 187–192, https://doi.org/10.1175/JAS-D-12-0189.1.

Thual, S., and A. J. Majda, 2015: A suite of skeleton models for the MJO with refined vertical structure. *Math. Climate Wea. Forecasting*, **1**, 70–95, https://doi.org/10.1515/mcwf-2015-0004.

——, and ——, 2016: A skeleton model for the MJO with refined vertical structure. *Climate Dyn.*, **46**, 2773–2786, https://doi.org/10.1007/s00382-015-2731-x.

——, ——, and S. N. Stechmann, 2014: A stochastic skeleton model for the MJO. *J. Atmos. Sci.*, **71**, 697–715, https://doi.org/10.1175/JAS-D-13-0186.1.

Wang, B., and H. Rui, 1990: Dynamics of the coupled moist Kelvin–Rossby wave on an equatorial β-plane. *J. Atmos. Sci.*, **47**, 397–413, https://doi.org/10.1175/1520-0469(1990)047<0397:DOTCMK>2.0.CO;2.

——, and T. Li, 1994: Convective interaction with boundary-layer dynamics in the development of a tropical intraseasonal system. *J. Atmos. Sci.*, **51**, 1386–1400, https://doi.org/10.1175/1520-0469(1994)051<1386:CIWBLD>2.0.CO;2.

——, and G. Chen, 2017: A general theoretical framework for understanding essential dynamics of Madden–Julian oscillation. *Climate Dyn.*, **49**, 2309–2328, https://doi.org/10.1007/s00382-016-3448-1.

——, and Coauthors, 2018: Dynamics-oriented diagnostics for the Madden–Julian oscillation. *J. Climate*, **31**, 3117–3135, https://doi.org/10.1175/JCLI-D-17-0332.1.

——, G. Chen, and F. Liu, 2019: Diversity of the Madden–Julian oscillation. *Sci. Adv.*, **5**, eaax0220, https://doi.org/10.1126/sciadv.aax0220.

Wang, L., and T. Li, 2020a: Effect of vertical moist static energy advection on MJO eastward propagation: Sensitivity to analysis domain. *Climate Dyn.*, **54**, 2029–2039, https://doi.org/10.1007/s00382-019-05101-8.

——, and ——, 2020b: Reexamining the MJO moisture mode theories with normalized phase evolutions. *J. Climate*, **33**, 8523–8536, https://doi.org/10.1175/JCLI-D-20-0202.1.

——, ——, E. Maloney, and B. Wang, 2017: Fundamental causes of propagating and non-propagating MJOs in MJOTF/GASS models. *J. Climate*, **30**, 3743–3769, https://doi.org/10.1175/JCLI-D-16-0765.1.

Wheeler, M. C., and G. N. Kiladis, 1999: Convectively coupled equatorial waves: Analysis of clouds and temperature in the wavenumber–frequency domain. *J. Atmos. Sci.*, **56**, 374–399, https://doi.org/10.1175/1520-0469(1999)056<0374:CCEWAO>2.0.CO;2.

——, and H. H. Hendon, 2004: An all-season real-time multivariate MJO index: Development of an index for monitoring and prediction. *Mon. Wea. Rev.*, **132**, 1917–1932, https://doi.org/10.1175/1520-0493(2004)132<1917:AARMMI>2.0.CO;2.

Yanai, M., S. Esbensen, and J. H. Chu, 1973: Determination of bulk properties of tropical cloud clusters from large-scale heat and moisture budgets. *J. Atmos. Sci.*, **30**, 611–627, https://doi.org/10.1175/1520-0469(1973)030<0611:DOBPOT>2.0.CO;2.

Yang, D., and A. P. Ingersoll, 2013: Triggered convection, gravity waves, and the MJO: A shallow-water model. *J. Atmos. Sci.*, **70**, 2476–2486, https://doi.org/10.1175/JAS-D-12-0255.1.

——, and ——, 2014: A theory of the MJO horizontal scale. *Geophys. Res. Lett.*, **41**, 1059–1064, https://doi.org/10.1002/2013GL058542.

Zhang, C., 2005: Madden-Julian oscillation. *Rev. Geophys.*, **43**, RG2003, https://doi.org/10.1029/2004RG000158.

——, and J. Ling, 2017: Barrier effect of the Indo-Pacific Maritime Continent on the MJO: Perspectives from tracking MJO precipitation. *J. Climate*, **30**, 3439–3459, https://doi.org/10.1175/JCLI-D-16-0614.1.

——, Á. F. Adames, B. Khouider, B. Wang, and D. Yang, 2020: Four theories of the Madden–Julian Oscillation. *Rev. Geophys.*, **58**, e2019RG000685, https://doi.org/10.1029/2019RG000685.

Zhang, G. J., and X. Song, 2009: Interaction of deep and shallow convection is key to Madden–Julian Oscillation simulation. *Geophys. Res. Lett.*, **36**, L09708, https://doi.org/10.1029/2009GL037340.

Zhu, Z., and T. Li, 2017: Statistical extended-range forecast of winter surface air temperature and extremely cold days over China. *Quart. J. Roy. Meteor. Soc.*, **143**, 1528–1538, https://doi.org/10.1002/qj.3023.